



Deposited via The University of Sheffield.

White Rose Research Online URL for this paper:

<https://eprints.whiterose.ac.uk/id/eprint/129623/>

Version: Accepted Version

Article:

Zhang, B. and Marshall, M.B. (2018) Investigating the Application of a Honeycomb Abradable Lining in the Turbine Stage of an Aero-Engine. *Tribology International*, 125. pp. 66-74. ISSN: 0301-679X

<https://doi.org/10.1016/j.triboint.2018.04.013>

Reuse

This article is distributed under the terms of the Creative Commons Attribution-NonCommercial-NoDerivs (CC BY-NC-ND) licence. This licence only allows you to download this work and share it with others as long as you credit the authors, but you can't change the article in any way or use it commercially. More information and the full terms of the licence here: <https://creativecommons.org/licenses/>

Takedown

If you consider content in White Rose Research Online to be in breach of UK law, please notify us by emailing eprints@whiterose.ac.uk including the URL of the record and the reason for the withdrawal request.

Abstract

1 Modern aero-engines use abrasible linings to reduce axial gas leakage. In this study the wear performance of a new
2 developed nickel superalloy honeycomb abrasible lining was investigated on a novel high-speed test rig, using in-situ
3 measurement techniques, combined with post-test microscopy and X-ray fluorescence based elemental analysis. In
4 particular the effect of changing the nickel-aluminide filler ratio was considered, as well as the impact of thermal
5 ageing of the specimens. Compaction of abrasible occurs, resulting in fin wear, along with high forces and
6 temperatures. This wear mechanism is cyclic with debris ejection and sparks. Ageing of the abrasible generally
7 leads to an increase in fin wear, with the exception that in one case this lead to improved fracture of the abrasible
8 and an improved cutting performance by the fin.
9

10
11
12
13
14
15
16
17
18
19
20
21
22
23
24
25
26
27
28
29
30
31
32
33
34
35
36
37
38
39
40
41
42
43
44
45
46
47
48
49
50
51
52
53
54
55
56
57
58
59
60
61
62
63
64
65

1 Introduction

1 In an aero engine, axial gas flow in the gaps between the rotating blade tips and the surrounding casing leads to
2 reduced thermal efficiency, causing increased operating costs and CO₂ emissions. Therefore aero engine operators
3 aim to minimise this gap and keep it as small as possible in order to minimise leakage. This is achieved by using
4 abradable linings [1], into which the blade tips cut, producing a seal for a given engine stage.
5

6 Abradable linings are applied in both the compressor and turbine stages of the engine with different sealing systems.
7 Generally, the compressor blade is in direct contact with the abradable lining, whereas a T-shaped tooth, which is
8 also called a turbine blade fin, is used to shroud the turbine blade. In the latter case, the tip of the tooth is in contact
9 with the lining. [2, 3]

10 Further, as aero-engines continue to develop, higher core temperatures are required to improve overall performance.
11 This leads to higher working temperatures in the turbine stage of the engine, and in particular in the high-pressure
12 turbine. These temperatures are beyond the operating limit of traditional thermally sprayed abradables [4, 5], and
13 honeycomb based materials have been developed, consisting of a nickel alloyed honeycomb structure and nickel-
14 aluminium filler [6, 7]. These materials have been designed to be resistive to the higher operating temperatures
15 required.
16

17 Recently, researchers have been investigating the use of abradables in aero-engines, with Oerlikon Metco focusing
18 on researching and manufacturing materials for gas turbine applications [3, 6, 7, 8]. They conducted a series of
19 studies investigating the use of different abradables such as aluminium-silicon and nickel based systems for different
20 coating applications. The performances of the different systems were linked to material properties, along with working
21 temperature and operating speed. In particular the wear mechanisms at each of these operating conditions were
22 identified. A series of studies have also been undertaken to characterize the wear mechanism between an abradable
23 lining and compressor blade using in-situ measurement techniques. These techniques have included stroboscopic
24 imaging to analyse the adhesive transfer between the blade tips and lining [9], as well as contact force measurement
25 [10], and have been used to investigate the effect of different blade tip treatments [11] and abradable hardness [12]
26 on the wear mechanics. Compared to compressor blade tip and abradable interactions, limited studies are available
27 with respect to sealing fins. Delebarre et al. investigated the fin seal system for an Inconel 718 triple-fin blade and Al-
28 Si abradable [13]. In their study, tests with low incursion rate showed cyclical behaviour in terms of force and material
29 removal; however no reason was given for this behaviour. Apart from this latter study, no other studies are present in
30 the literature on sealing fins.
31

32 The aim of this study is to explore the wear mechanism between Inconel 718 fins and nickel-aluminium honeycomb
33 abradables, by evaluating the wear behaviour during an incursion test. In particular the effect of the filler composition
34 will be investigated, as well as the impact of thermal ageing on the samples. Post-test, microscope and X-ray
35 fluorescence (XRF) analysis will be used on the rub area in order to understand the wear mechanism between the fin
36 tip and different honeycomb abradables, and combined with the in-situ measurements.
37

2 Material and Method

2.1 Test rig

38
39
40
41 This study uses a test rig previously developed at the University of Sheffield to study the wear mechanism between
42 aero-engine linings and compressor blades or turbine fin tips [14]. The rig consists of a rotating disc driven by a high-
43 speed spindle, and a microscope stage (OptoSigma SHOT-202, Laser2000 UK Ltd., Northants, UK) onto which the
44 abradable sample is mounted (Figure 1a). Within the disc two fin samples are mounted, with one being used as the
45 sample for test, and the other a dummy for balancing. The spindle is capable of rotating the disc up to speeds of
46 21000RPM, with this corresponding to a blade tip speed of 200ms⁻¹. Similarly, the microscope stage can operate with
47 a linear speed between 0.1 and 2000 μms⁻¹. The rig is operated by a customized Labview programme, and an
48 incursion event is created by moving the abradable sample towards the rotating disc at a set speed, until a
49 prescribed depth is reached.
50
51
52
53
54
55
56
57
58
59
60
61
62
63
64
65

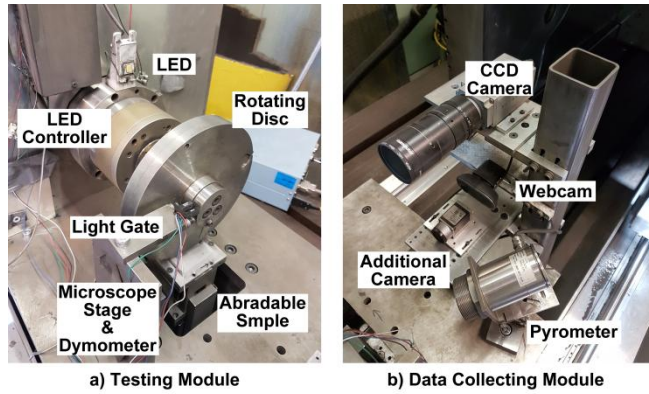


Figure 1 Testing & Data Collect modules on test rig

The sensor system on the test rig (Figure 1b) consists of a CCD camera (Pixelink PL-B741U, Scorpion Vision Ltd., Hants., UK), a webcam (Logitech C90, Logitech International S.A., Switzerland), a dynamometer (3-Component Force Link Type 9317C, Kistler Instruments Ltd. UK) and a pyrometer (Optris CTXL3MH1-CF3, Optris GmbH, Germany). The CCD camera uses an LED stroboscopic imaging system (9) to capture the fin profile during the test, and is powered by an impulse power source. A small metal arm fixed onto the rotating disc interrupts a light gate linked to the imaging system, and in this way the timing of the flash can be set, and the camera used to capture an image of the fin when it passes top dead centre. Additionally, the webcam takes video of the sparks and the screenshots are saved automatically every 50ms by the LabView programme. The dynamometer is installed under the abrasible sample. It measures the force magnitude during the test and transfers the signal to the computer. Finally, the inferred pyrometer focuses on the abrasible samples and passes the real-time temperature reading of the wear area to the computer.

2.2 Test sample and test parameters

The abrasible samples used in this study consisted of a nickel superalloy honeycomb structure with nickel aluminide filler (Figure 2a). The first three samples were in the un-aged condition and had a standard, nickel rich and aluminium rich filler respectively. The nickel-aluminium powder, which is also called nickel aluminide, has two phases, NiAl and Ni₃Al; and these phases shift with different nickel contents [15]. Generally, Ni₃Al is harder and has lower thermal conductivity than NiAl [16-18], and it is also important to note that NiAl transforms to Ni₃Al under high temperature [19]. The standard filler has a Ni-Al weight ratio of 86%-14% [5], which is typically used in aero-engines. The second set of samples have the same honeycomb structure and filler combinations, but this time are in the aged condition, to compare the effect of the ageing process. The ageing process is conducted by heating as-manufactured samples continually for 100 hours under 1000°C to simulate the real-life engine working environment. Following exposure to high temperature, the nickel aluminide is oxidised and produces NiAl₂O₄ [20]. NiAl₂O₄ has a spinel structure that leads to a very high level of hardness and very low thermal conductivities [21, 22].

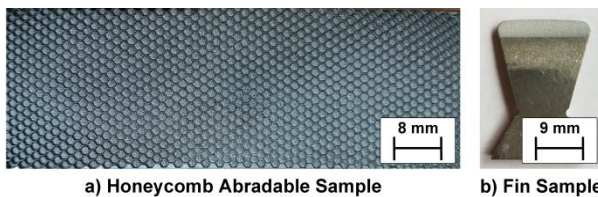


Figure 2 Standard un-aged honeycomb abrasible and HVOF coated Inconel 718 Fin

The fin sample (Figure 2b) used in this study is made from Inconel 718, is 30mm in length, flat with 3mm thickness, and with the fin tip tapered to 1.3mm to simulate the turbine fin geometry. Generally, the turbine blades and the sealing fins in aero-engines are made from Inconel 718, which is the same as the material used in this study. Additionally, the samples are coated with ZrO₂ by a HVOF coating method in order to emulate the real aero-engine. In an aero-engine, the turbine blades are usually coated by different coating materials for different aims. The most common coating type is a thermal barrier coating, which can protect the blade fin from thermal damage. ZrO₂ combined with Al₂O₃ is a common thermal barrier coating material due to its low thermal conductivity [23]. This coating material can be coated onto the blade fin surface by using plasma electrolytic oxidation [24] or high velocity oxygen fuel spraying (HVOF) [25].

Test Code	Fin Type	Abrasible	Tip Speed [m/s]	Incursion speed [µm/s]	Incursion Rate [µm/pass]	Incursion Depth [µm]
-----------	----------	-----------	-----------------	------------------------	--------------------------	----------------------

Test - S	IN718-HVOF	Standard	200	62.1	0.2	2500
Test - A,S	IN718-HVOF	Aged standard	200	62.1	0.2	2500
Test - Al+	IN718-HVOF	Aluminium rich	200	62.1	0.2	2500
Test - A,Al+	IN718-HVOF	Aged aluminium rich	200	62.1	0.2	2500
Test - Ni+	IN718-HVOF	Nickel rich	200	62.1	0.2	2500
Test - A,Ni+	IN718-HVOF	Aged nickel rich	200	62.1	0.2	2500

Table 1 Designed testing parameters

As previously introduced, this study is focused on how the abradable filler properties affect the wear mechanism between the fin tip and abradable. Additionally, according to previous research, the tip speed and incursion speed are two dominant parameters with respect to the wear mechanism but the incursion depth is not a dominant test parameter [9-12]. Therefore, all the tests are conducted with a tip speed of 200ms^{-1} and incursion speed of $62.1\mu\text{ms}^{-1}$. It should be noted that the incursion speed is selected to represent the incursion rate of $0.2\mu\text{m/pass}$ that was used in previous research [10, 12] and is aero-engine representative. The incursion depth for this study was set at $2500\mu\text{m}$ to ensure that the test duration is sufficient for collecting data that would allow full analysis of the wear mechanism. Table 1 shows the test conditions of each test, with a test code for the nickel-aluminium content (S: standard, Al+: aluminium rich and Ni+: nickel rich) and ageing condition (A: aged) used to label all tables and figures in this paper.

2.3 Test procedure and data processing

As previously detailed, there are two slots on the rotation disc for fitting the fin samples. The dummy fin sample, made from IN718 is 3mm shorter than the testing sample, and was fixed onto the rotation disc by clamps in one slot. The fin sample to be tested is then fitted into the other slot. After the abradable is fixed on the microscope stage, the test is conducted. During the test, all test conditions are controlled by the LabView programme. Additionally, the programme captures live videos from the webcam cameras and saves the frames individually for post-processing. The data from the dynamometer and pyrometer is also saved individually in a text format with a timestamp.

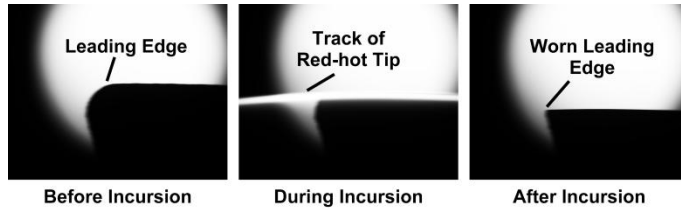


Figure 3 Fin profile during testing

The change in the length of the fin can be determined by analysing the images captured by the CCD camera (Figure 3). Each image contains four or five exposures of the fin tip profile due to the high rotation speed, as it is much higher than the camera stroboscopic frequency. The other set of images captured come from the fin-abradable contact and show the interaction. As the honeycomb abradable is relatively hard, a spark is generated by the wear process, and shown on the webcam monitor (Figure 4) with data captured at a frequency of 50ms.

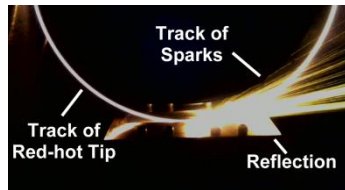


Figure 4 Sparking during testing with aged standard abradable

Since the fin is running in a circular route during the test, the force magnitude in the axial direction is always zero. Therefore, the dynamometer outputs two sets of force data, which represent the radial (normal) and tangential force components. The dynamometer outputs are processed into a single data set that presents the force change against time by extracting the maximum force recorded from each strike. In a similar manner, temperature data is also recorded as a function of time.

Wear occurs as the fin passes over the abradable surface, with the arc of contact increasing as the incursion depth of the fin into the abradable increases. As the time for each rotation of the disc is constant during the test, the total rub length does not linearly relate to the test time. Therefore in order to compare the results, the total rub length was calculated, as this is reflective of the work done by the fin on the abradable, and is calculated as follows:

$$L = \sum_{i=1}^n \cos^{-1} \left(\frac{r - \text{incursionrate} \times i \times 10^{-6}}{r} \right) \times r$$

where L is counted total rub length (m), r is the fin disk radius (m), and i is the number of pass

All outputs obtained from the test rig are processed into five individual characteristic variables, fin length, normal force, tangential force, temperature and sparks change along with the total rub length.

The worn groove is also investigated post-test. To study the difference between each groove, microscopic and X-Ray fluorescence (XRF) analyses were employed on the worn groove surface. The microscope used was a Carl Zeiss Imager A1.M optical microscope with 5.0x zoom-in coefficient, with three images taken (one in the middle point and two at the end points) of each wear scar. The XRF test was conducted using a Fischerscope X-Ray fluorescence machine (Fischerscope X-Ray XAN-250, Fischer Technology Inc., USA), which detects the elemental content of a material sample surface within a small round area of 1.2mm diameter. To reduce the error, ten sample points are randomly taken from the detecting surface for repeat testing and the result is the average value of these ten data sets. Finally, the test samples were sectioned at the middle of the wear groove to analyse the sub-surface structure.

3 Results

During the testing procedure, the incursion depth was changed twice (Table 2). As mentioned in the previous section, the incursion depth was originally set at 2500µm. However, during testing of both the standard and aged standard abrasives high fin wear was detected, and led to the disc becoming unbalanced. Therefore for the two subsequent tests, the incursion depth was reduced to 1000µm, in order to avoid damage to the spindle. After testing the two aluminium rich abrasives at this depth, the incursion depth was increased to 1500µm for the remaining two nickel rich abrasive samples, as the level of expected fin wear was now understood. Increasing the test duration led to more data being collected. However, upon analysis it was determined that all tests, even those of shorter durations, had run for a sufficient amount of time to be both steady state and create a data set that could be fully analysed.

Test Code	Fin Type	Abradable	Tip Speed [ms ⁻¹]	Incursion Rate [µm/pass]	Incursion Depth [µm]
Test - S	IN718-HVOF	Standard	200	0.2	2500
Test - A,S	IN718-HVOF	Aged standard	200	0.2	2500
Test - Al+	IN718-HVOF	Aluminium rich	200	0.2	1000
Test - A,Al+	IN718-HVOF	Aged aluminium rich	200	0.2	<1000
Test - Ni+	IN718-HVOF	Nickel rich	200	0.2	1500
Test - A,Ni+	IN718-HVOF	Aged nickel rich	200	0.2	1500

Table 2 Actual testing parameters

3.1 Worn groove analysis

The most direct evidence for determining the wear performance during the test is the worn groove. Figure 5 shows the wear scar on each of the abrasives and fins after the test. Also marked on the figure is the expected groove length in each case, and by comparing this to the actual groove length achieved, an indication of wear can be seen. Where the worn groove is similar in value to that expected, fin wear was low, and where the actual groove is significantly shortened, high wear is observed. As shown in the Figure 5, the performance of the standard, aged standard and aged nickel rich abrasives was poor during the test, and that the only test to achieve close to the expected groove length was the un-aged nickel rich sample.

1
2
3
4
5
6
7
8
9
10
11
12
13
14
15
16
17
18
19
20
21
22
23
24
25
26
27
28
29
30
31
32
33
34
35
36
37
38
39
40
41
42
43
44
45
46
47
48
49
50
51
52
53
54
55
56
57
58
59
60
61
62
63
64
65

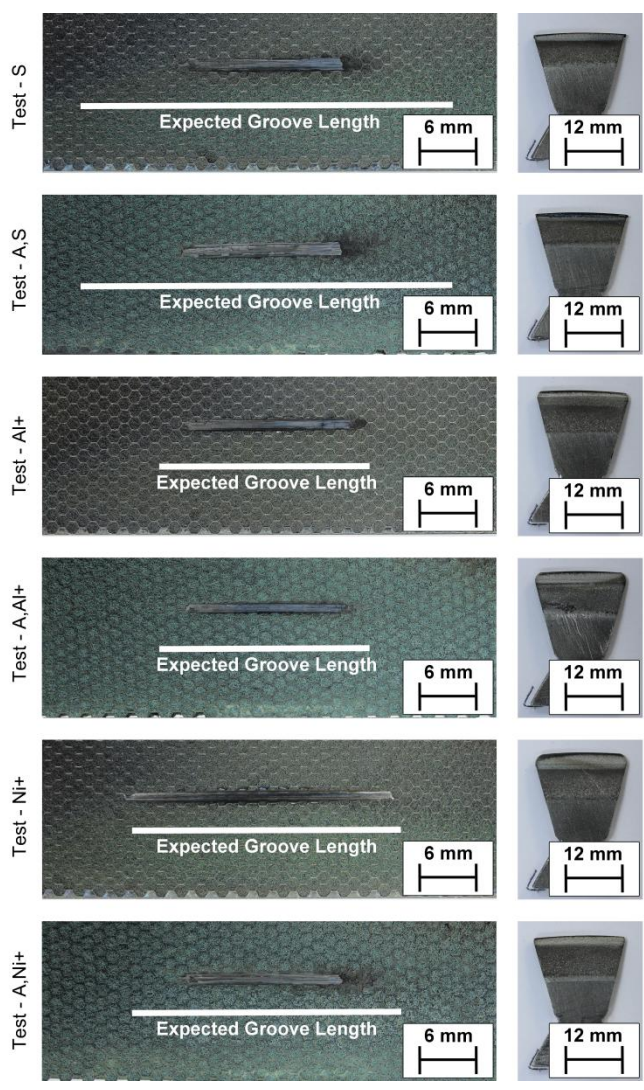


Figure 5 Worn groove and fin profile after testing

3.2 In-cycle measurements

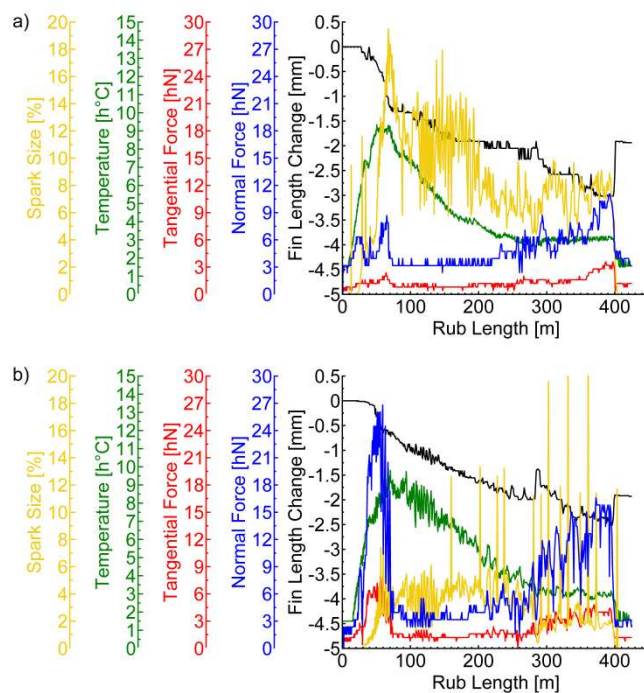


Figure 6 Test results for standard abrasives, a) Test - S b) Test – A,S

Figure 6 shows the fin length change, force (normal and tangential), temperature and spark results from the standard and the aged-standard tests. These results have been selected as they contain features typical of the different incursion tests. As shown, after the start of the test the force and temperature at the contact point increase and reach a peak value around a rub length of 50 to 60 meters. During this event the fin length begins to shorten, and just prior to the force and temperature reducing, a spark (represented by the spark size) is released. As shown in Figure 6b, in some cases cyclic behaviour is also observed with this process repeated periodically during the test. In other cases, as shown Figure 6a, the test is more stable with less peaks in the force and temperature data. However, in the latter case it should be noted that sparks continue to be emitted.

When comparing across the different tests, for the un-aged abrasible the most significant sparking was observed in the standard case, with this being accompanied by the largest blade length change. At the other extreme, the nickel rich abrasible was extremely consistent with comparatively low forces and temperatures (650°C), with negligible blade wear and sparking observed. In the case of the aged abrasibles, forces and temperatures were higher than when compared to the un-aged case, with an increased tendency for cyclic behaviour. An exception was the test with the aged aluminium rich specimen, where no sparking was observed, and fin wear was minimal (Figure 5).

3.3 Post-processed results

Further numerical analysis was applied to all the incursion test results in order to compare the different tests more directly. The fin wear condition was quantitatively analysed by measuring the fin length and weight before and after the test (shown in Figure 7). However, as noted, the total rub lengths were different between tests, meaning that further processing of results was required to make a valid comparison. Previous research has shown that material loss is proportional to rub length for abrasible material [10]. Therefore in order to compare between the six tests, the fin length and weight change was normalised with respect to total rub length, and is similarly shown on Figure 7. As shown in Figure 7, both standard and aged standard abrasibles suffer significant wear damage as does the aged nickel rich one. It should also be noted that even though there is no fin length change observed after the test with nickel rich abrasible, the fin weight is slightly reduced. As shown in Figure 5, in this case the loss of material can be seen on the leading edge of the fin tip, where the tip coating is slightly removed due to wear. As a general point, the fins tested with aluminium rich abrasibles tend to experience less wear, with this especially true for the aged case.

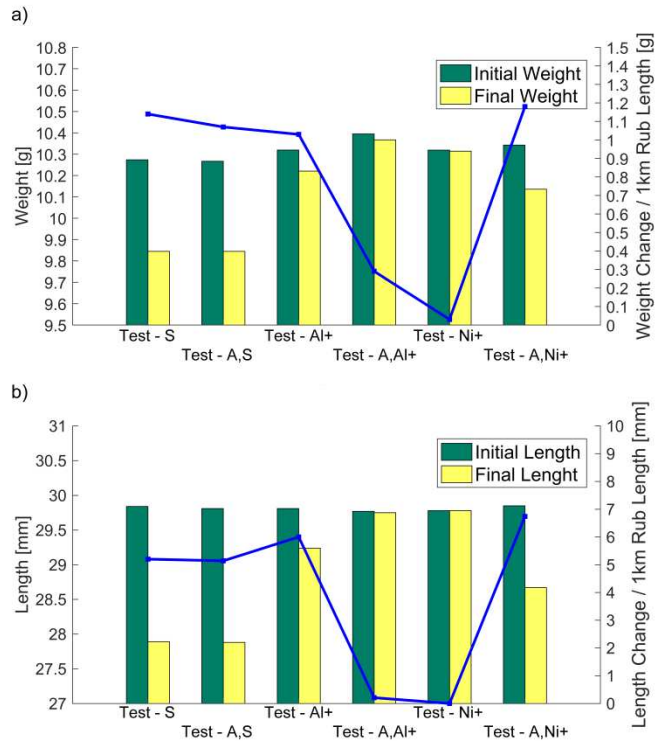


Figure 7 Fin weight change before and after incursion test

The maximum force and temperature data were extracted from the steady state test results to evaluate the difference between each test (Figure 8). With regards to force, it can be observed that the maximum tangential forces of the tests with aged abrasives are higher than the un-aged ones. The temperature results also suggest that more frictional heating is generated during the tests with aged abrasives. It is also interesting to note that there is more variation in the force results for the aged abrasives than compared to the un-aged case; where with the exception of the normal force for the standard un-aged abrasive, normal forces are similar for all the filler types, as are the tangential forces.

As will be discussed later, the link between force and temperature is complicated, as changing the aluminium-nickel ratio in the filler changes the thermal diffusivity and mechanical properties. For example, the nickel rich abrasive has relatively high forces, but lower temperatures when compared to the other tests. However, what is clear is that upon ageing a given abrasive, both the force and temperature rise, suggesting that additional frictional heating occurs.

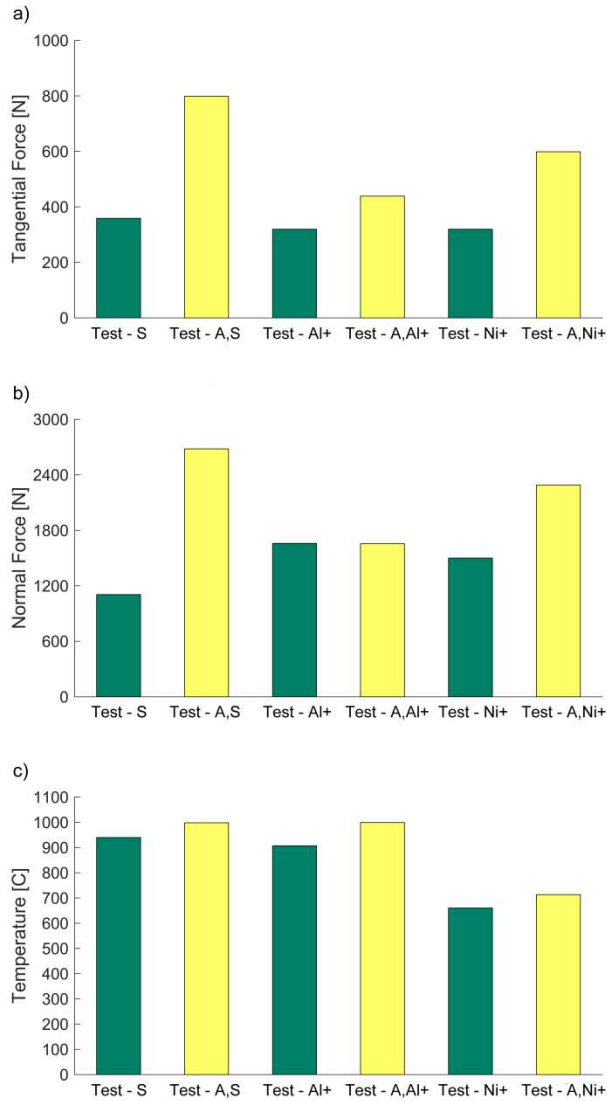


Figure 8 Comparison of maximum force and temperature

4 Post-test characterization

4.1 Worn groove surface micrographic analysis

Whilst the variable rub lengths in the tests created the need for further processing of the fin length and weight change results, this was not an issue when analysing the wear scars as in each case the wear mechanism was fully developed. Figure 9 shows the microscope images of the different surfaces of the worn grooves. It can be seen that compared to the other three worn grooves, those of the aluminium rich, aged aluminium rich and nickel rich abrasives are relatively smooth and shiny. Additionally, data from the incursion test results shows that these three abrasives have lower fin wear. On the other hand, the worn grooves of the standard, aged standard and aged nickel rich abrasives are rough; these worn grooves contain shiny and dark surfaces. It was also observed during the microscope analysis that the shiny layer is above the dark layer. Finally, all of the worn grooves have areas containing blue-purple marks on the surface, which represent thermal damage to the material.

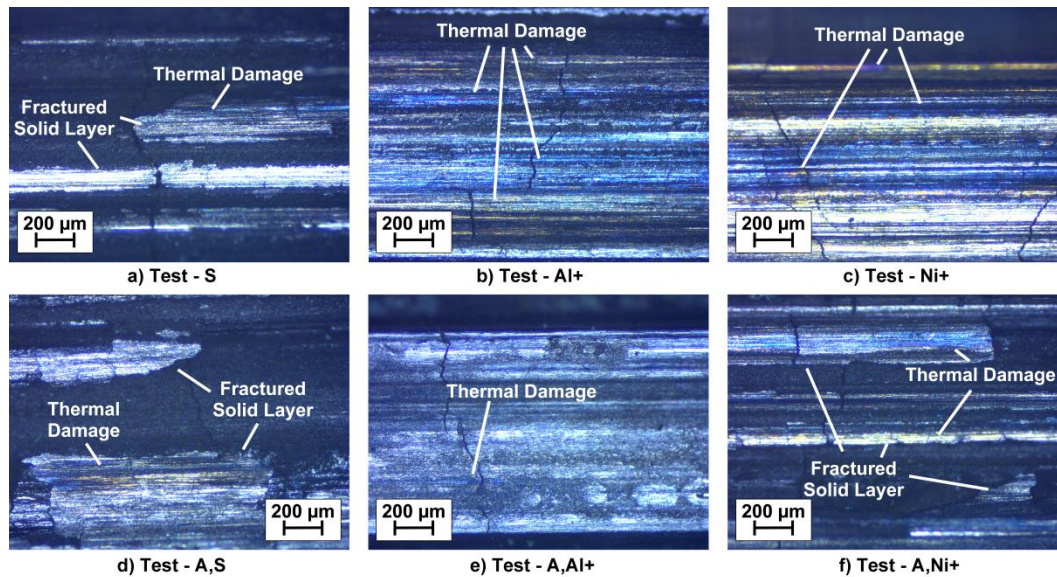


Figure 9 Microscopies (5.0x) of worn grooves surface

4.2 X-ray fluorescence (XRF)

XRF investigation (Table 3) of the fin and the abrasible samples highlighted that nickel and zirconium can be defined as characteristic elements, and used to determine whether the rub track on a sample is material from the abrasible or also made up of transfer from the fin. As shown in the Table 3, the abrasible sample is made up of over 90% nickel, compared to 47% for the base material of the fin, with the only source of zirconium being the fin tip. As previously highlighted, a smooth surface to some degree is seen in all of the samples apart from the un-aged Nickel rich one. The rub tracks on these samples contain a mixture of nickel and zirconium, with the nickel concentration being at a lower percentage than the base abrasible. This indicates that the smooth surface is a consolidated mixture of the abrasible and the fin material. As was also mentioned, the groove surface on the nickel rich abrasible is unique. The elemental distribution of this sample is very close to that of base abrasible material, indicating negligible transfer from the fin in this case.

Test Code	Ti	Cr	Fe	Co	Ni ¹	Cu	Zr	Nb	Mo	Ta	Balance
Test - S	0.81	14.35	17.92	1.21	57.75	0.08	0.68	4.16	2.78	0.26	0.00
Test - A,S	0.97	18.03	18.09	0.56	53.12	0.09	0.83	5.61	2.52	0.19	-0.01
Test - Al+	0.96	19.74	18.11	0.64	50.22	0.08	2.00	5.58	2.48	0.20	-0.01
Test - A,Al+	1.39	25.16	14.71	1.71	47.89	0.16	3.14	3.72	1.81	0.31	0.00
Test - Ni+	0.00	3.51	3.34	0.38	90.19	0.06	0.00	0.05	1.92	0.27	0.28
Test - A,Ni+	0.97	18.23	17.77	1.03	52.03	0.07	1.34	6.00	2.39	0.18	-0.01
Fin Base	0.95	16.69	17.33	0.17	47.53	8.17	0.17	5.45	3.07	0.48	-0.01
Fin Tip	0.00	1.27	0.00	2.61	3.37	0.07	82.66	0.00	0.51	0.00	9.51
Abradable ²	0.04	5.36	1.65	0.23	90.46	0.08	0.00	0.05	1.87	0.29	-0.03

Table 3 XRF results for abrasible groove surface, blade and un-tested abrasible

4.3 Worn groove sectional micrographic analysis

The test samples were also sectioned, with Figure 10 presenting the sectioned views of the worn grooves from each test. As shown in the Figure 10, the aged samples are significantly discoloured due to oxidation, when compared to their un-aged counterparts. For the un-aged samples, the morphology of the grooves shows there are two main components in each case, a surface layer of consolidated material that may or may not be partially removed, with a sub-layer of compressed filler beneath it. However, it should also be noted that the nickel rich sample is unusual in the sense that the surface layer negligible with minimum compaction of the filler. This result is in line with the XRF measurement for this sample (see section 4.2), where the elemental distribution was close to that of the base material. Comparing the standard and aluminium rich specimens, in the former case the consolidated layer is prone to fracture and removal, whereas in the latter case higher levels of distortion are present with a more continuous layer formed.

¹Fischerscope® X-Ray XAN®-250 cannot detect aluminium element therefore the nickel content in the table represents sum of aluminium and nickel content.

²The abrasible XRF result present the average value of six different abrasible

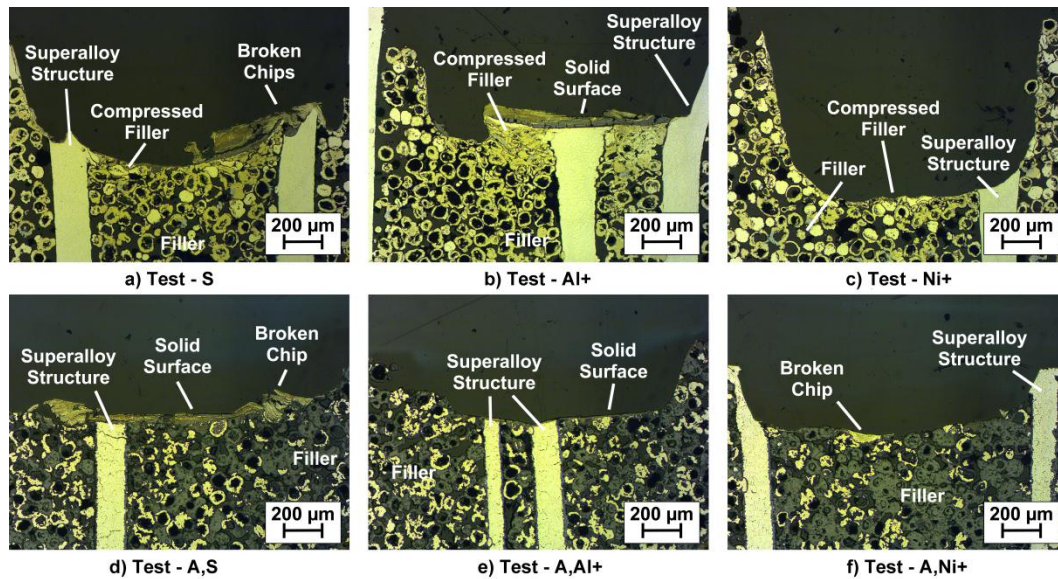


Figure 10 Microscopies (5.0x) of sectional viewing of worn grooves

For the aged samples, with the exception of the aged standard case, the surface layer is less significant, with the compressed layer also less apparent. Indeed, whilst evident from the images of the rub tracks (Figure 9), the consolidated layer is only really evident in the sectioned view of the aged standard abrasible. It is also interesting to note, for this sample as in the un-aged case, fracture and removal of the consolidated layer occurs. With respect to the aluminium and nickel rich aged specimens, the consolidated material is minimal, and confined to a very thin surface layer, although as highlighted by the XRF measurements, fin transfer occurs.

5 Discussion

The results of the incursion tests give both insights into the mechanism of material removal, as well as showing clear differences between each condition investigated. In this section the material removal mechanism will be discussed, as well as the influence of both the nickel-aluminium ratio in the filler and ageing.

5.1 Material removal mechanism

As highlighted in the results section, cyclic behaviour in terms of force and temperature has been observed, coupled with sparking. This behaviour occurred in the tests with standard, aged standard and aged nickel rich abrasibles, and was similar in nature to that observed in previous studies [13]. As shown by the microscope images in section 4.1, the groove surfaces on these abrasibles is coarse, with the microscopic images presented in section 4.3 suggesting that this type of surface is made up of two layers. The upper layer is shiny, with XRF results suggesting that the shiny layer is consolidated material from both the abrasible and fin tip. The lower layer is rough, and has a relatively dark colour, and has been identified as the filler in a compressed powder form. Further, the fractured nature of the upper layer also indicates it cracks and periodically peels off, resulting in the observed coarsely worn surface.

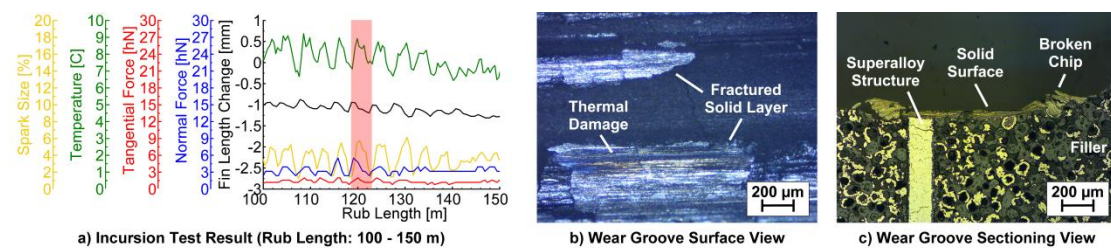


Figure 11 General results of incursion test with aged standard abrasible

Combining these observations with the cyclic force and temperature behaviour recorded during tests, the sparking mechanism can be divided into four steps, and is summarised in Figure 11. Taking the aged standard abrasible as an example, initially the fin tip touches the abrasible surface and the abrasible is compacted. This results in high forces and frictional heating as the material is compressed, leading to a hard dense metal layer containing a mixture of fin and abrasible material. As the incursion progresses, force and temperature continue to rise, until at a certain point ductility in the compacted layer is exceeded and fracture occurs. The solid surface then splits into small hot chips and is peeled away due to the high forces, resulting in sparks. The ejection of material then leads to a gap,

1 force and temperature reduce, and consolidation re-initiates, with this process repeatable over the duration of the
2 test. In the cases where this process does not occur or is lesser in severity, such as the nickel rich case, it is due to
3 fracture of the abrasible and an absence of consolidating behaviour.

4 **5.2 Influence of Ni/Al ratio & ageing**

5 As highlighted in the results section a range of different behaviours were observed for the honeycomb samples.
6 Significant differences were observed linked to the Ni-Al ratio as well as whether the samples were aged or not. As
7 previously highlighted, the abrasible filler is a nickel-aluminium powder that creates a Ni-Al matrix system. In a Ni-Al
8 matrix system, changing the Ni-Al ratio leads to significantly different material properties [15]. For un-aged (as
9 manufactured) abrasibles, a higher nickel concentration gives an increased percentage of Ni₃Al, while a higher
10 aluminium concentration leads to a higher percentage of NiAl [15], with the standard case having a mixture of the
11 two. These changes are significant, as Ni₃Al in particular is hard, brittle, and has poor thermal diffusivity [18].

12 The effect of these changes is evident in the test samples. In the case of the standard sample, forces and
13 temperatures are relatively high, with significant compaction and brittle fracture of the consolidated layer. When the
14 aluminium ratio is increased, as in the aluminium rich case, the softer abrasible consolidates significantly more
15 (Figure 10b). Whilst it might be expected that temperatures and forces are reduced compared to the standard case,
16 as the material is softer and with increased thermal diffusivity [17], this is not the case. The increased level of
17 consolidation leads to significant push back and frictional heating, resulting in higher fin wear, force and temperatures
18 than seen for the standard ratio. With regards to fin wear, temperature is a significant factor, as Inconel 718 will
19 soften at temperatures over 700°C [26], highlighting why wear may be higher for the softer aluminium rich case.
20 Conversely, it might be expected that for the nickel rich case, the harder filler of lower thermal diffusivity will be
21 worse. However, as observed, good fracture of the abrasible occurs with little consolidation (Figure 10c). Whilst
22 forces are still relatively high due to the hardness of the filler, temperatures and fin wear are reduced in the absence
23 of a significantly compacted layer. This latter case highlights how the compacted layer drives the wear mechanics of
24 the system.

25 Further changes occur to the nickel-aluminium filler with ageing, as the filler oxidises. Upon oxidation, both NiO and a
26 spinel structured NiAl₂O₄ phase are generated [20]. The NiAl₂O₄ phase in particular is of increased hardness, brittle
27 and of reduced thermal diffusivity [21]. Generally ageing leads to a decrease in wear performance, as the abrasible
28 is now harder, except in the aluminium rich case where a change in mechanism occurs.

29 In the case of the standard aged sample, it has mixture of NiO and NiAl₂O₄ phases, leading to high forces and
30 temperatures, along with fin wear. For the aluminium rich aged specimen wear is reduced. In this case, the increased
31 aluminium ratio leads to a higher concentration of the NiAl₂O₄ phase. As this phase is relatively brittle, increased
32 fracture of the abrasible occurs and consolidation is reduced. Whilst temperatures are relatively high due to the poor
33 thermal diffusivity of this material, driving some blade wear, forces are lower due to the absence of significant
34 consolidation, and the overall performance improved when compared to the standard case. Finally, for the nickel rich
35 aged sample, the NiO phase dominates, and is accompanied by high forces and moderate temperatures, with
36 temperatures reduced compared to the standard case due to the improved thermal diffusivity of NiO compared to
37 NiAl₂O₄.

38 Overall the ability of the filler to fracture has the most significant impact on the performance of the honeycomb
39 aluminium-nickel filled abrasible system. In the un-aged case, the nickel rich sample fractures well and shows the
40 best performance, whereas in the aged condition this occurs in the aluminium rich case. As the abrasible ages in the
41 engine, the aluminium rich abrasible offers the best long term performance, however, pre-ageing is required in order
42 to avoid negative wear performance during initial running of the engine.

43 **6 Conclusions**

44 This project mainly studied the wear mechanism between the IN718-HVOF blade and different nickel-aluminium
45 based abrasibles. The results from the wear test and the other analyses show that:

- 46 - The fin typically compacts the abrasible, frequently leading to a dense surface. This surface layer leads to high
47 forces and temperatures, and ultimately fractures resulting in the release of sparks on a cyclic basis.
- 48 - Different Ni-Al content of the filler leads to different hardness and brittleness which affects the fracture
49 behaviour of the abrasible. Generally, the fin is less worn when the abrasible is easy to fracture.
- 50 - The ageing process hardens the abrasible samples and changes the thermal diffusivity, resulting in changes
51 to the wear mechanisms observed then compared to un-aged tests.
- 52 - High aluminium content makes abrasible hard to fracture under as-manufactured condition but easy to fracture
53 after ageing.

REFERENCES

- [1] D. Sporer, A. Refke, M. Dratwinski, M. Dorfman, Sulzer Metco plc., I. Giovannetti, M. Giannozzi, M. Bigi, GE Oil&Gas plc., New high-temperature seal system - Increased efficiency of gas turbine. 2008, Sulzer Technical Review, 2/2008. DOI: 10.1016/S1350-4789(08)70517-8
- [2] W. Dalzell, S. Sanders, G. Crawford, F. Walden, W. Woodard, Abradable seal with improved properties. US 6352264, USA, 2002.
- [3] S. Wilson OerlikonMetco, Thermally sprayed abradable coating technology for sealing in gas turbines. 2012, Brussels. Available at: https://www.oerlikon.com/ecomaXL/files/oerlikon_ThermallySprayedAbradableCoatings_2012.10.pdf&download=1 [Accessed 5 Mar. 2018].
- [4] Oerlikon Metco, Material Product Data Sheet - Aluminum Silicon Hexagonal Boron Nitride Abradable. 2014. Available at: https://www.oerlikon.com/ecomaXL/files/oerlikon_DSMTS-0017.3_AISi-hBN.pdf&download=1 [Accessed 5 Mar. 2018].
- [5] Oerlikon Metco, Material Product Data Sheet - Aluminum Silicon Polymer Thermal Spray Powders. 2016. Available at: https://www.oerlikon.com/ecomaXL/files/metco/oerlikon_DSMTS-0016.6_AISi-Poly.pdf&download=1 [Accessed 5 Mar. 2018].
- [6] Oerlikon Metco AG, Improve efficiency and reduce emissions with high pressure turbine abradable coatings for industrial gas turbines. 2014. SF-0015.1.
- [7] Oerlikon Metco, Material Product Data Sheet - Nickel Aluminum for Sintered Abradable Honeycomb Fillers. 2014. Available at: https://www.oerlikon.com/ecomaXL/files/oerlikon_DSMB-0051.4_NiAl_Honeycomb.pdf&download=1 [Accessed 5 Mar. 2018].
- [8] Sulzer Metco Plc., Solutions Flash - Improve efficiency and reduce emissions with high pressure turbine abradable coatings for industrial gas turbines. 2012. Available at: https://www.oerlikon.com/ecomaXL/files/oerlikon_SF-0015.1_IGT_HPT_Abradables_EN.pdf&download=1 [Accessed 5 Mar. 2018].
- [9] N. Fois, J. Stringer, J and M. Marshall, Adhesive transfer in aero-engine abradable linings contact, 2013, Wear, Vol. 304, No. 1-2, pp. 202-210. DOI: 10.1016/j.wear.2013.04.033
- [10] N. Fois, M. Watson, J. Stringer, M. Marshall, An investigation of the relationship between wear and contact force for abradable materials. 2014, Proceedings of the Institution of Mechanical Engineers, Part J: Journal of Engineering Tribology, Vol. 229, No. 2, pp. 136-150. DOI: 10.1177/1350650114545139
- [11] M. Watson, N. Fois, M. Marshall, Effects of blade surface treatments in tip-shroud abradable contacts, 2015, Wear, Vol. 338-339, pp. 268-281. DOI: 10.1016/j.wear.2015.06.018
- [12] N. Fois, M. Watson, M. Marshall, The influence of material properties on the wear of abradable materials, 2016, Proceedings of the Institution of Mechanical Engineers, Part J: Journal of Engineering Tribology. DOI: 10.1177/1350650116649528
- [13] C. Delebarre, V. Wagner, J. Paris, G. Desein, J. Denape, J. Gurt-Santanach, An experimental study of the high speed interaction between a labyrinth seal and an abradable coating in a turbo-engine application. 2014, Wear, Vol. 316, No. 1-2, pp. 109-118. DOI: 10.1016/j.wear.2014.04.023
- [14] J. Stringer, M. Marshall, High speed wear testing of an abradable coating. 2012, Wear, Vol. 294-295, pp. 257-263. DOI: 10.1016/j.wear.2012.07.009
- [15] G. Dey, Physical metallurgy of nickel aluminides, 2003, Sadhana, Vol. 28, No. 1-2, pp. 247-262. DOI: 10.1007/BF02717135
- [16] D. Kaliński, M. Chmielewski, K. Pietrzak, Mechanical, thermal and tribological properties of hot-pressed NiAl-Al₂O₃ composites. 2012, 15th European conference on composite materials, ECCM15.
- [17] J. Guo, Z. Wang, L. Sheng, L. Zhou, C. Yuan, Z. Chen, Z. L. Song, Wear properties of NiAl based materials. 2012, Progress in Natural Science: Materials International, Vol. 22, No. 5, pp. 414-425. DOI: 10.1016/j.pnsc.2012.10.008
- [18] P. Jozwik, W. Polkowski, Z. Bojar, Applications of Ni₃Al Based Intermetallic Alloys—Current Stage and Potential Perceptivities, 2015, Materials, Vol. 8, No. 5, pp. 2537-2568. DOI: 10.3390/ma8052537

1 [19] Y. Tamarin, Protective coatings for turbine blades. 2002, Materials Park, Ohio: ASM International, pp. 86. ISBN:
2 978-0-87170-759-8

3 [20] E. Loginova, F. Cosandey, T. Madey, Nanoscopic nickel aluminate spinel (NiAl_2O_4) formation during NiAl (111)
4 oxidation, 2007, Surface Science, Vol. 601, No. 3, pp L11-L14. DOI: 10.1016/j.susc.2006.11.047

5 [21] Y. He, K. Shih, Nano-indentation on nickel aluminate spinel and the influence of acid and alkaline attacks on the
6 spinel surface, 2012, Ceramics International, Vol. 38, No. 4, pp. 3121-3128. DOI: 10.1016/j.ceramint.2011.12.013

7 [22] J. Zygmuntowicz, P. Wiecińska, A. Miazga, K. Konopka, Characterization of composites containing NiAl_2O_4 spinel
8 phase from $\text{Al}_2\text{O}_3/\text{NiO}$ and $\text{Al}_2\text{O}_3/\text{Ni}$ systems. 2016, Journal of Thermal Analysis and Calorimetry, Vol. 125, No. 3,
9 pp. 1079-1086. DOI: 10.1007/s10973-016-5357-2

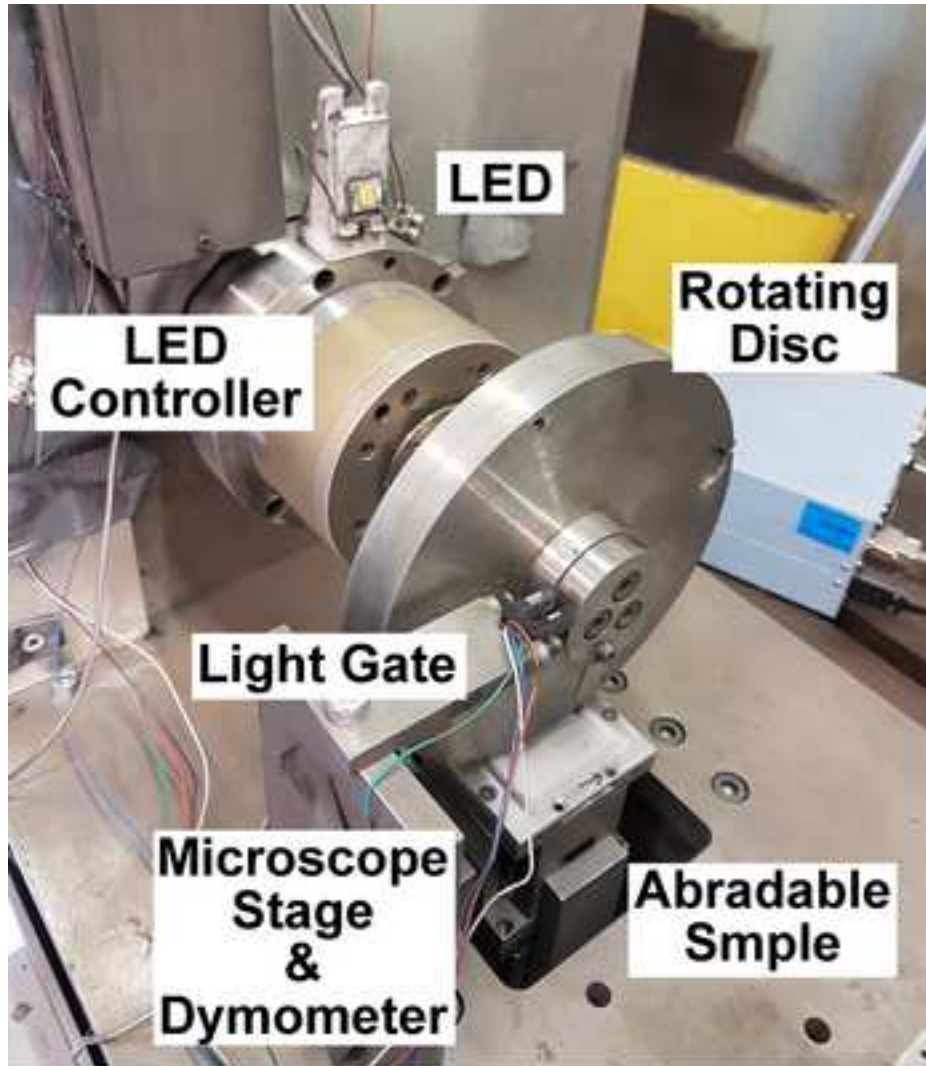
10 [23] J. Hostaša, W. Pabst, J. Matějček, Thermal Conductivity of $\text{Al}_2\text{O}_3\text{-ZrO}_2$ Composite Ceramics, 2011, Journal of
11 the American Ceramic Society, Vol. 94, No. 12, pp. 4404-4409. DOI: 10.1111/j.1551-2916.2011.04875.x

12 [24] T. Akatsu, T. Kato, Y. Shinoda, F. Wakai, Thermal barrier coating made of porous zirconium oxide on a nickel-
13 based single crystal superalloy formed by plasma electrolytic oxidation, 2013, Surface and Coatings Technology,
14 Vol. 223, pp. 47-51. DOI: 10.1016/j.surfcoat.2013.02.026

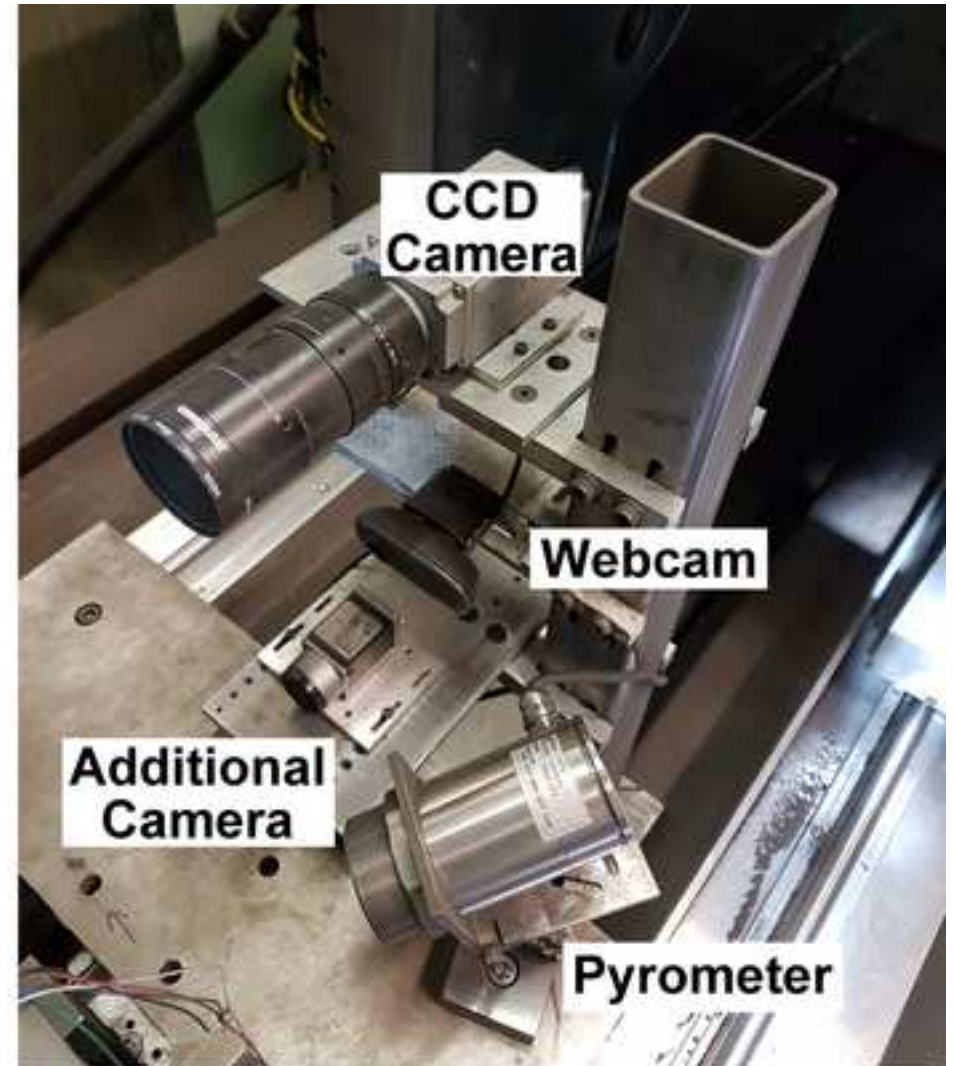
15 [25] T. Dobbins, R. Knight, M. Mayo, HVOF Thermal Spray Deposited Y_2O_3 -Stabilized ZrO_2 Coatings for Thermal
16 Barrier Applications, 2003, Journal of Thermal Spray Technology, Vol. 12, No. 2, pp. 214-225. DOI:
17 10.1361/105996303770348320

18 [26] Special Metals, Product handbook of high-performance alloys, 2008.
19
20
21
22
23
24
25
26
27
28
29
30
31
32
33
34
35
36
37
38
39
40
41
42
43
44
45
46
47
48
49
50
51
52
53
54
55
56
57
58
59
60
61
62
63
64
65

Figure 1



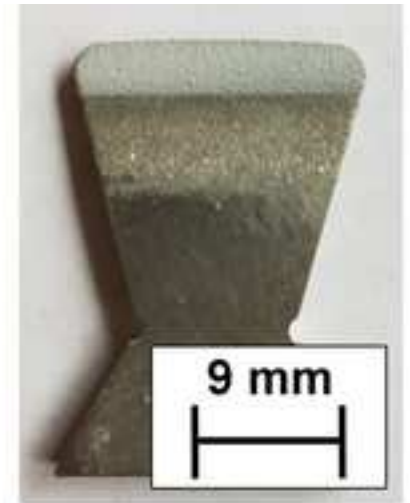
a) Testing Module



b) Data Collecting Module



a) Honeycomb Abradable Sample



b) Fin Sample

Figure 3

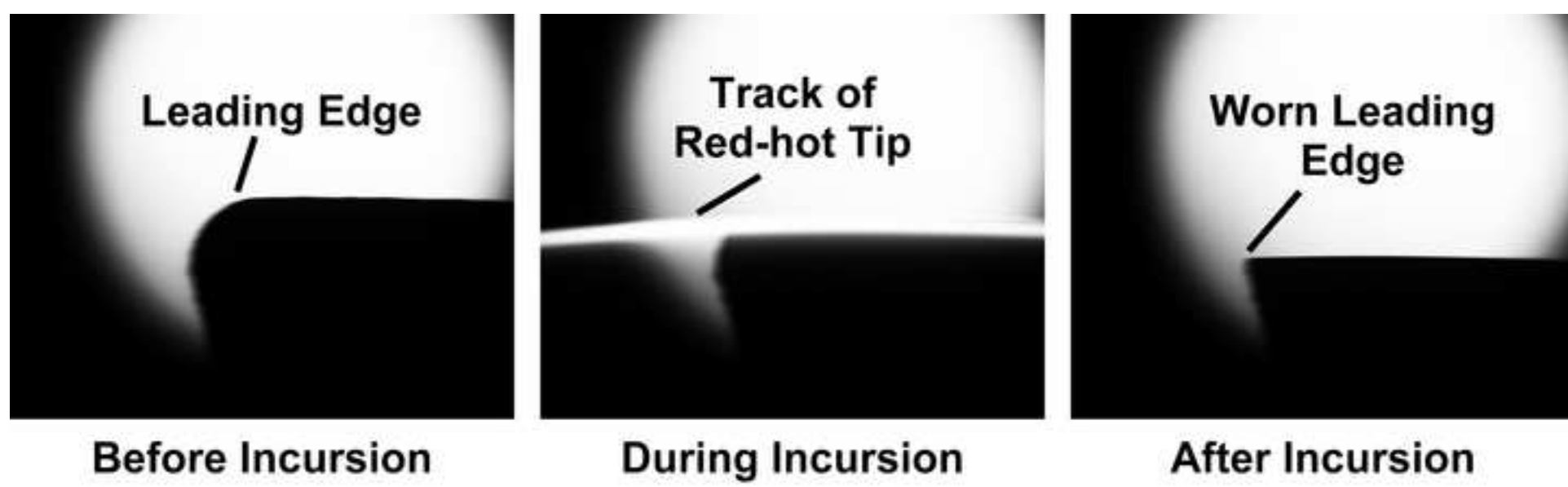


Figure 4

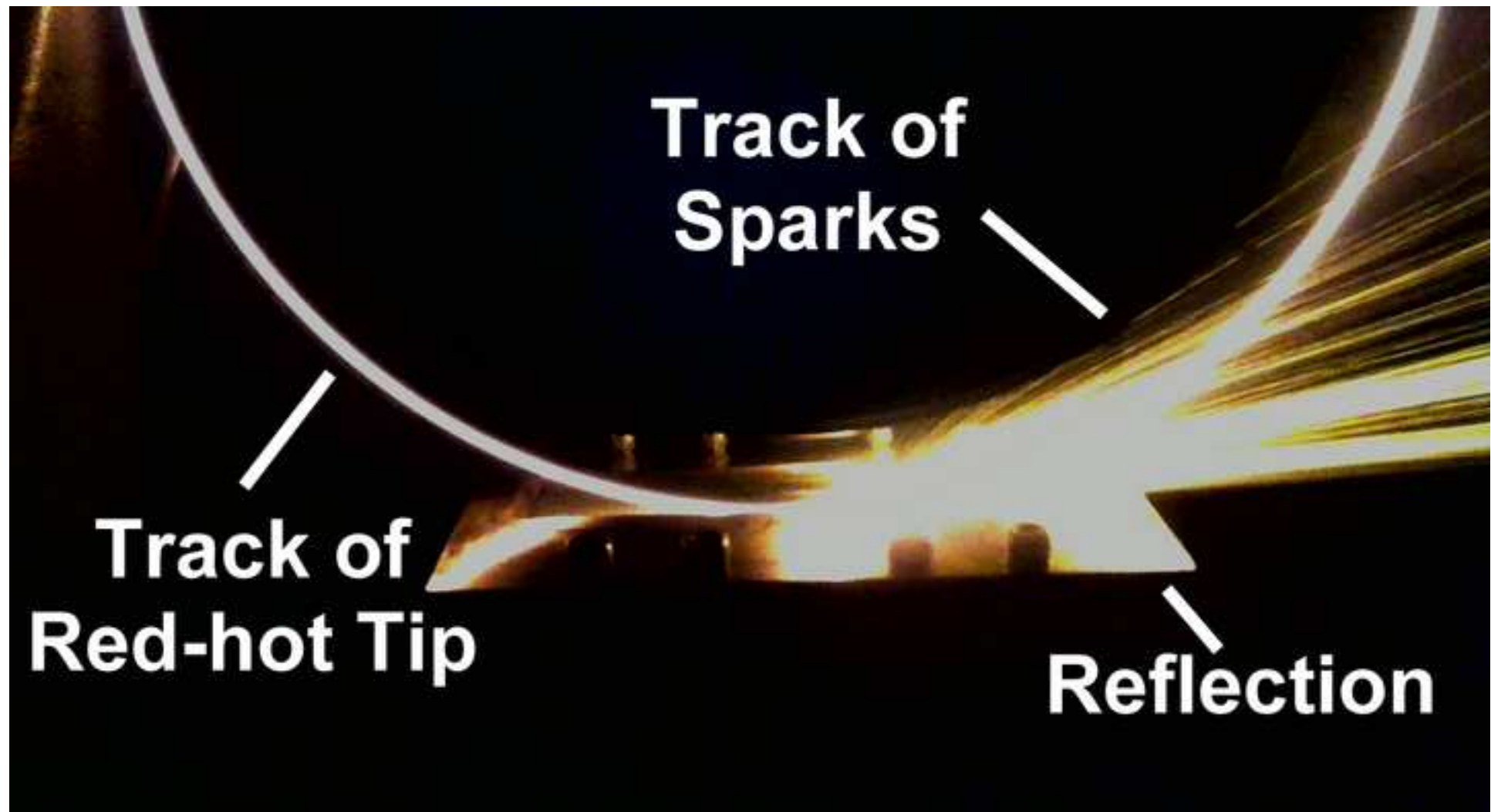


Figure 5

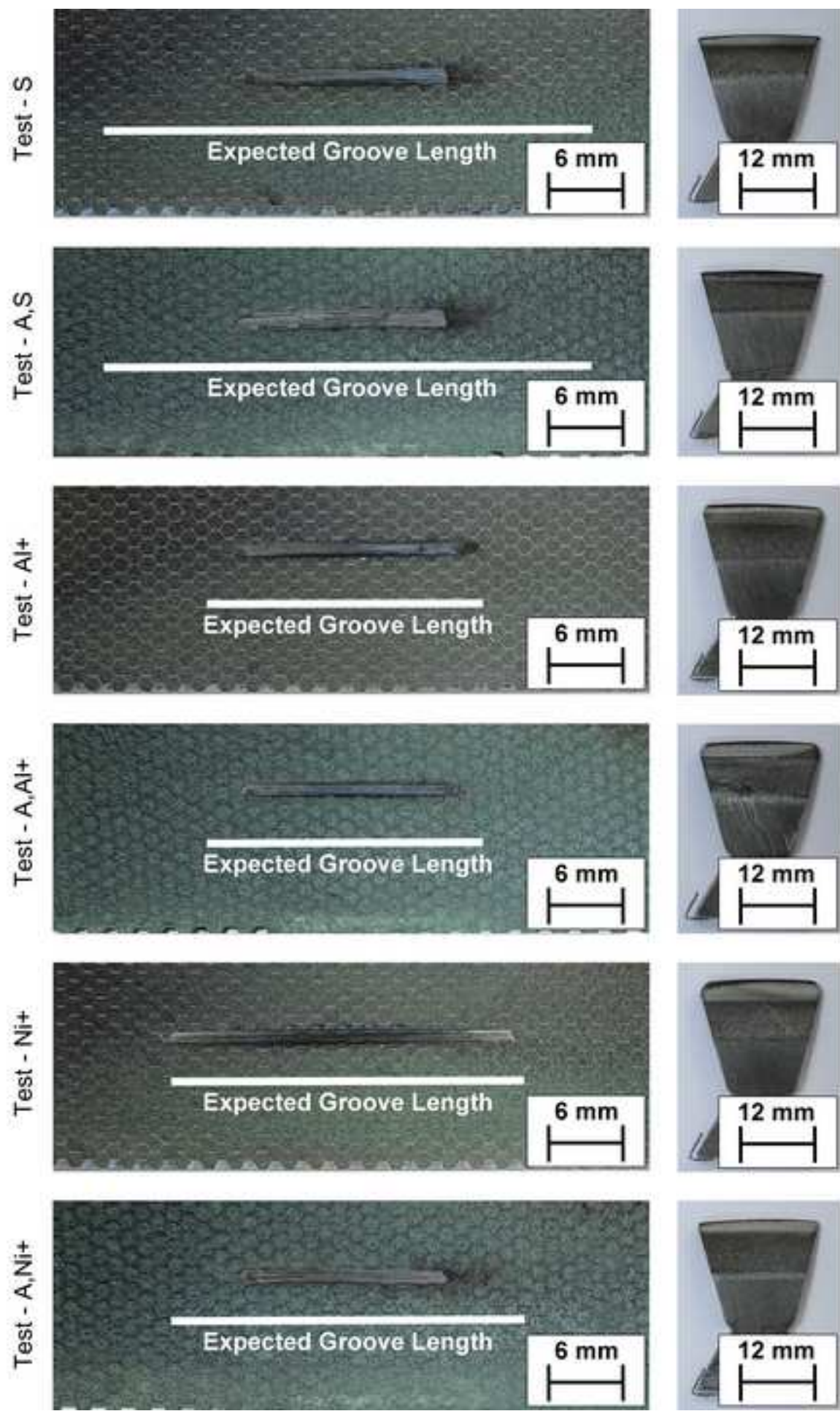


Figure 6

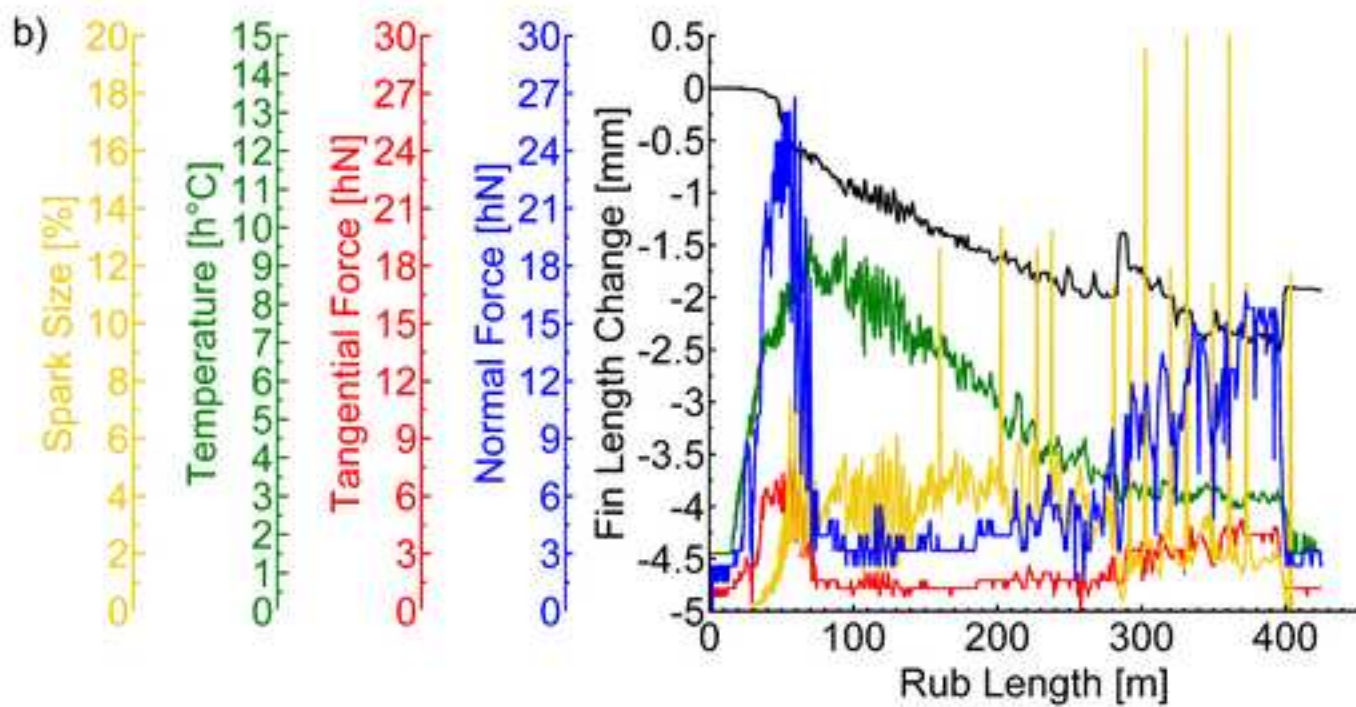
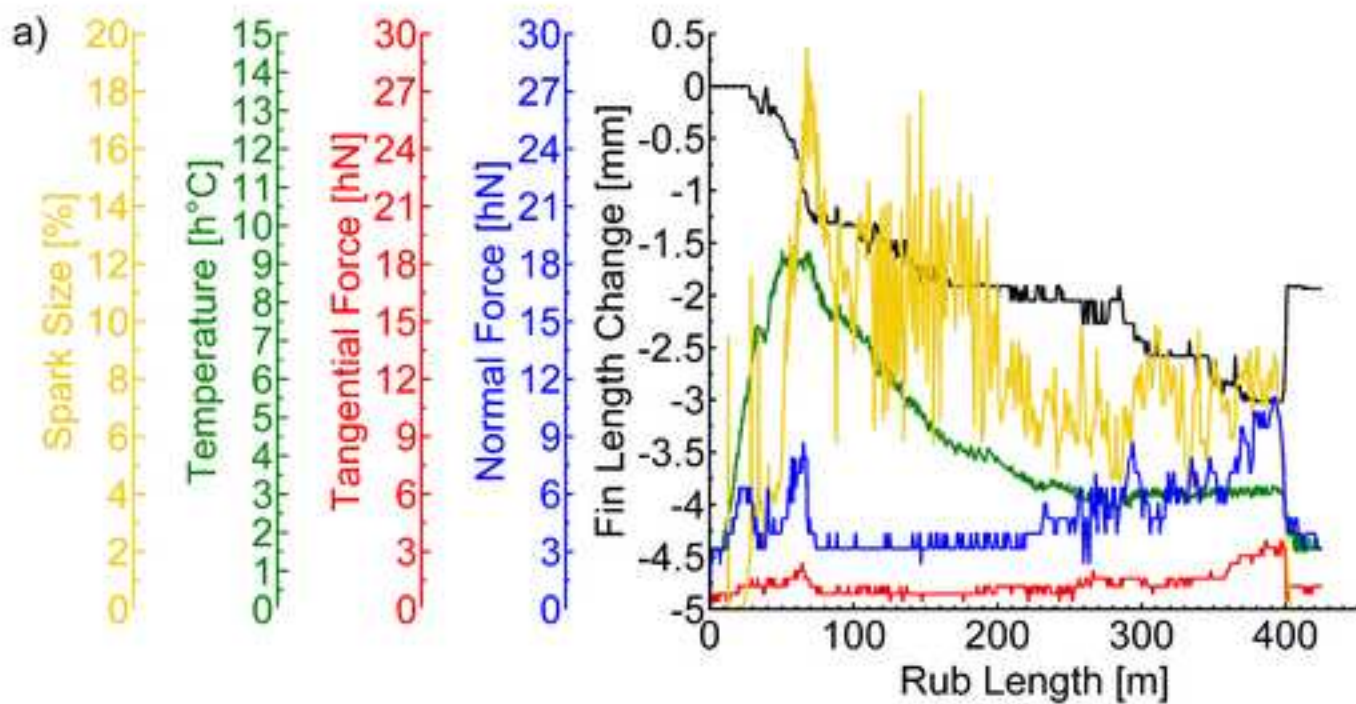
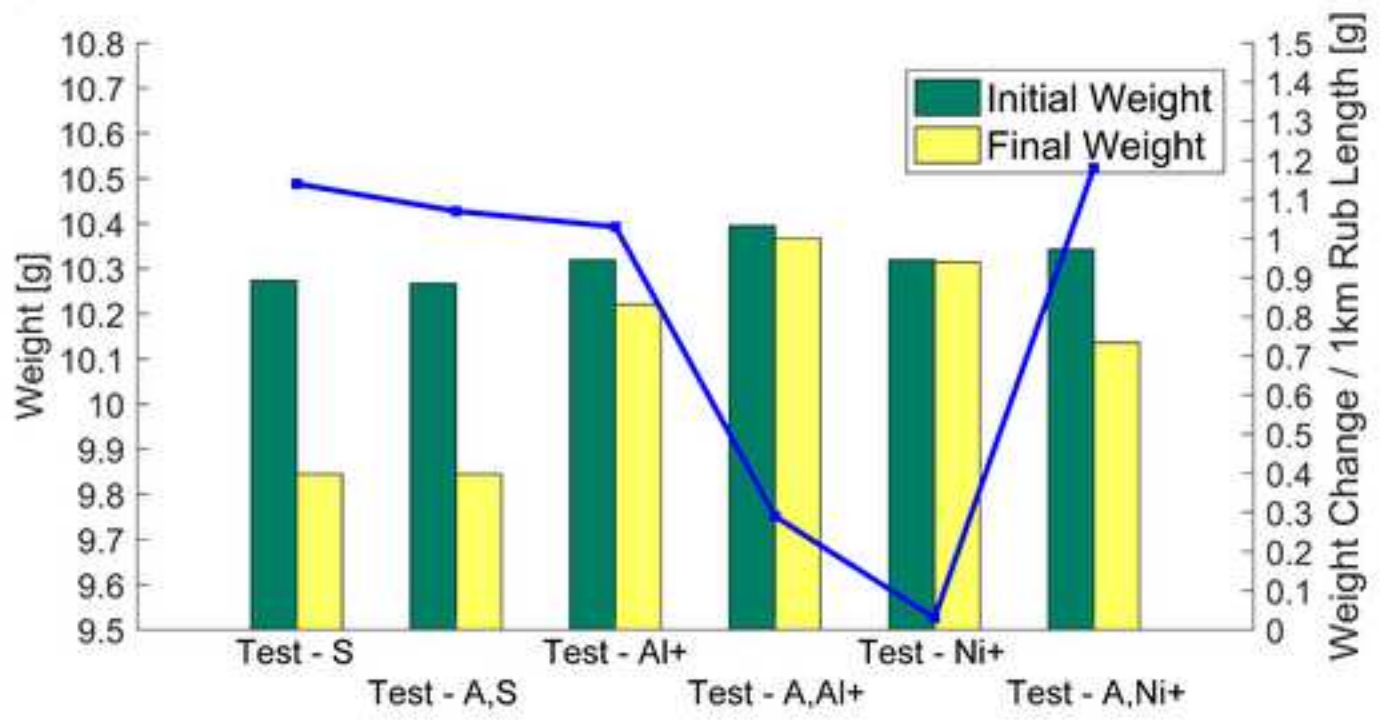


Figure 7

a)



b)

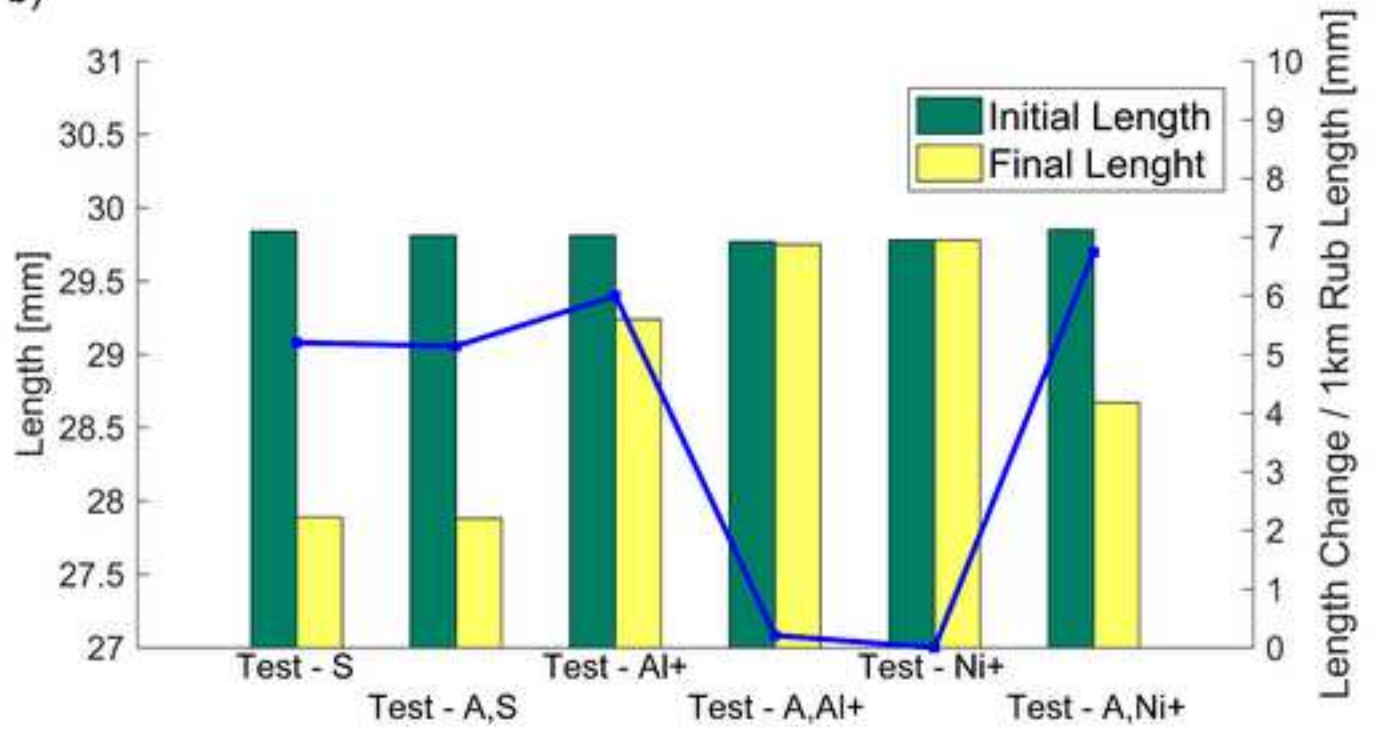


Figure 8

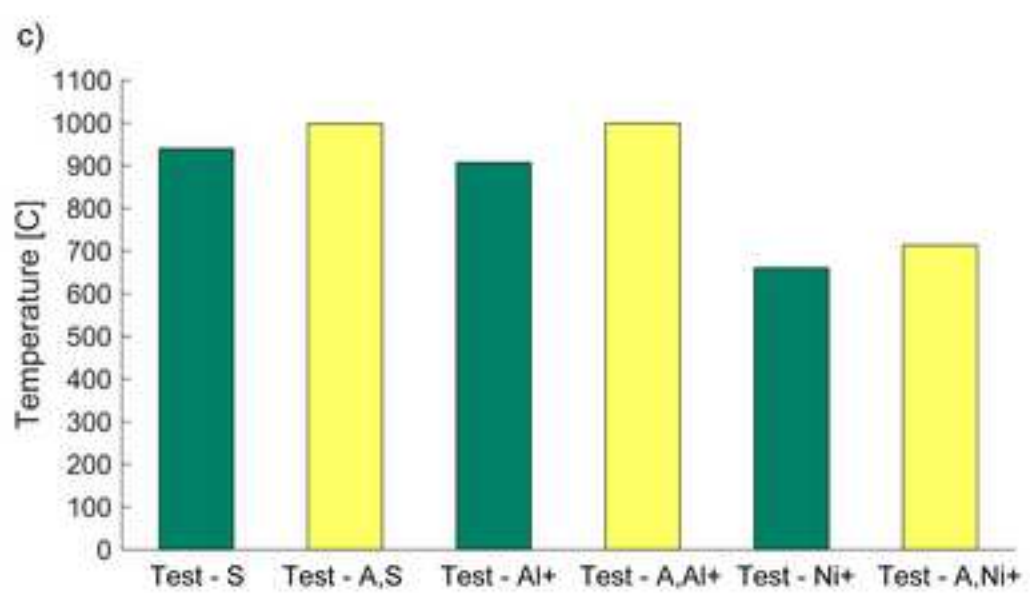
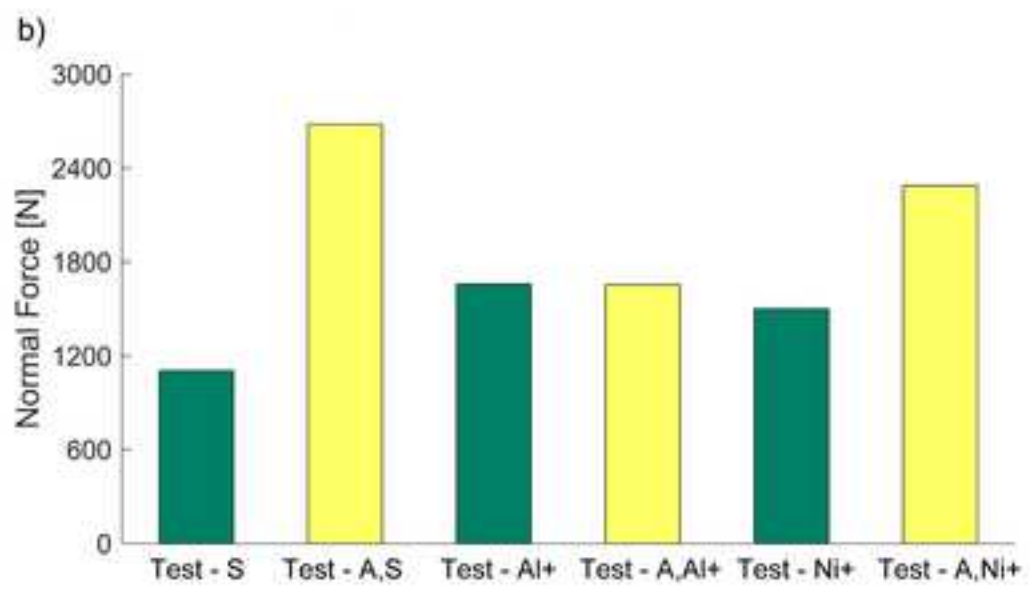
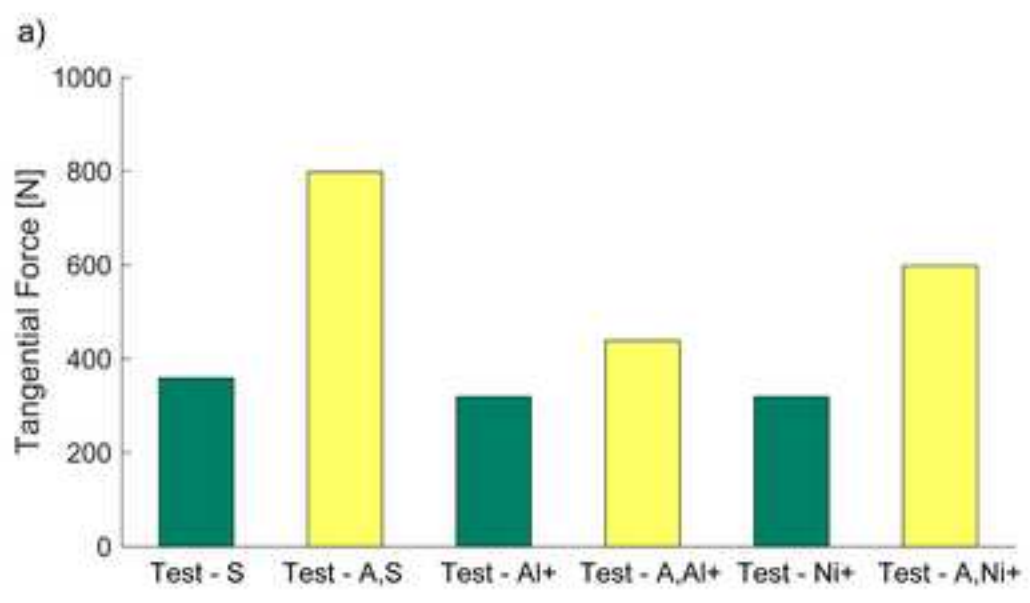
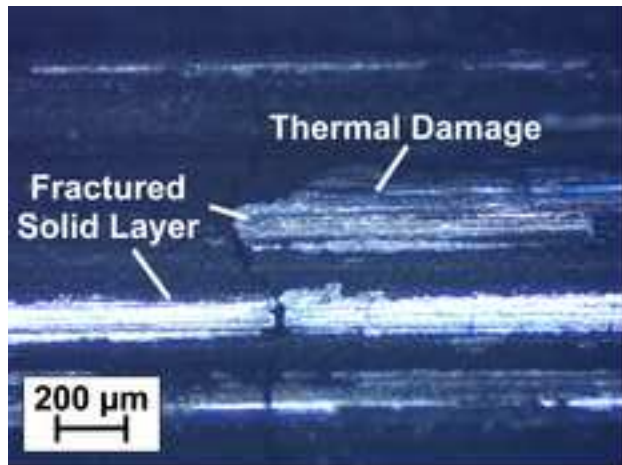
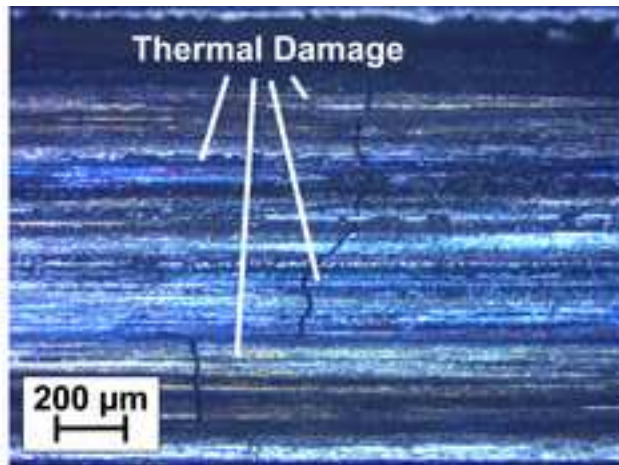


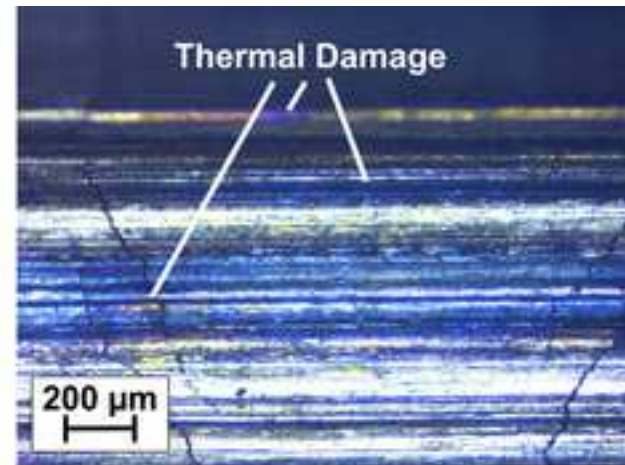
Figure 9



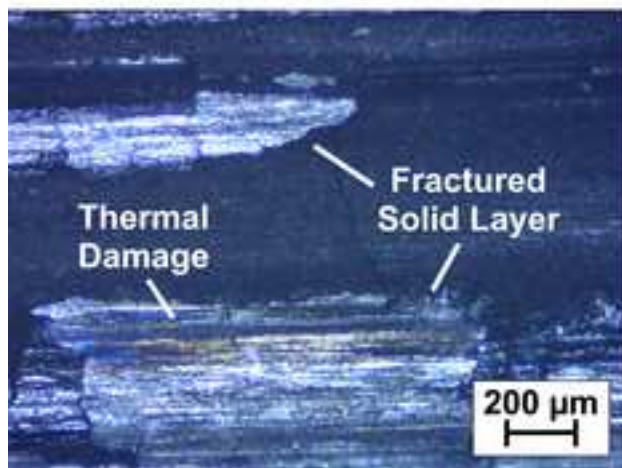
a) Test - S



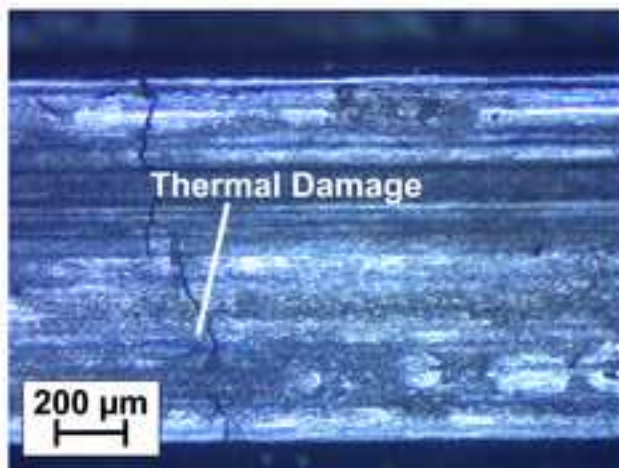
b) Test - Al+



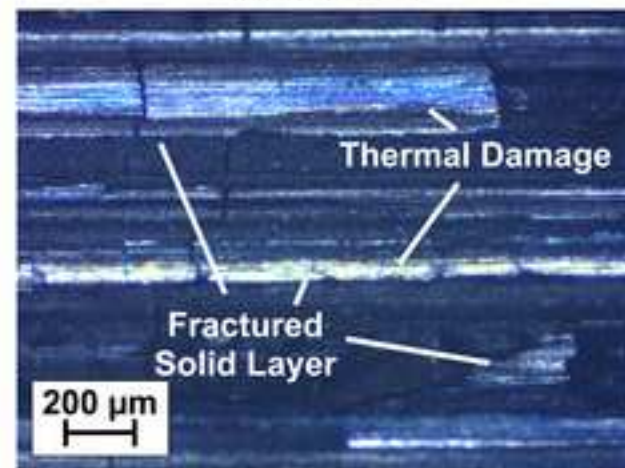
c) Test - Ni+



d) Test - A,S

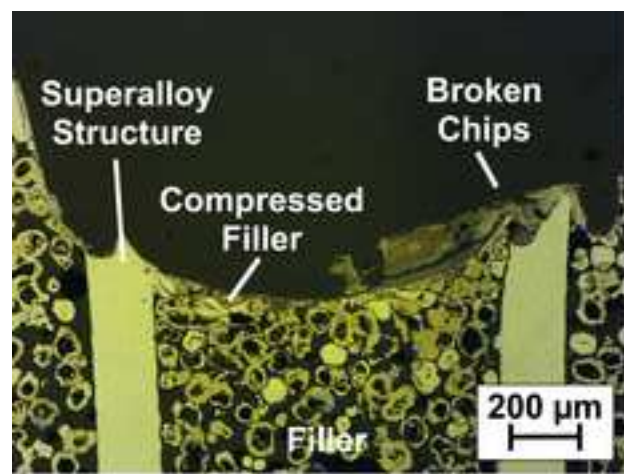


e) Test - A,Al+

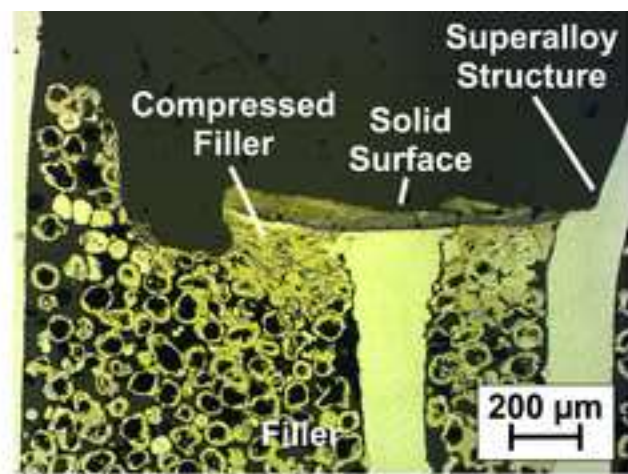


f) Test - A,Ni+

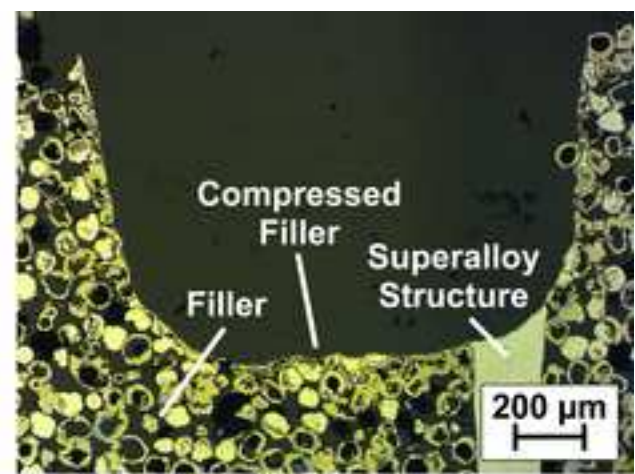
Figure 10



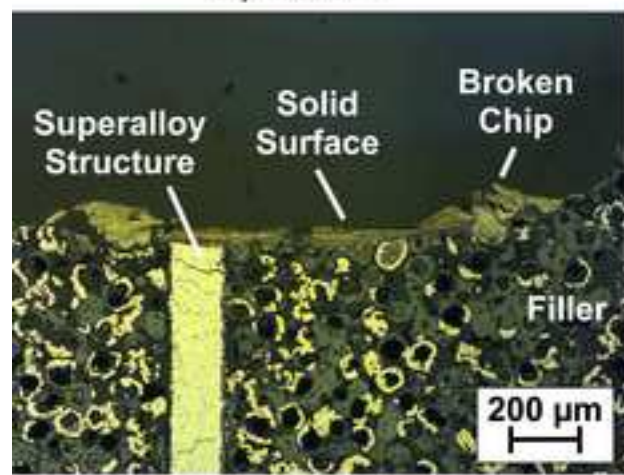
a) Test - S



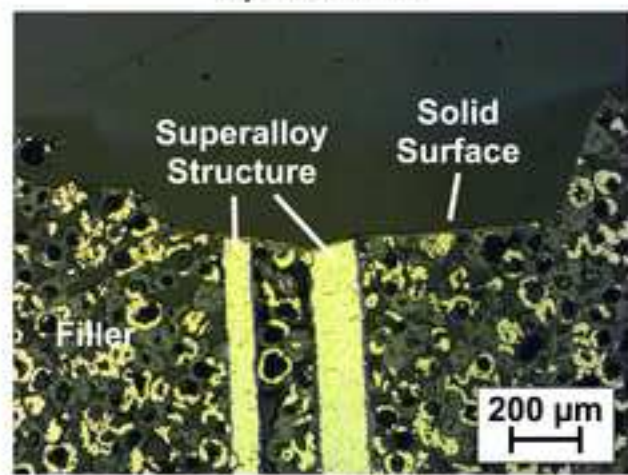
b) Test - Al+



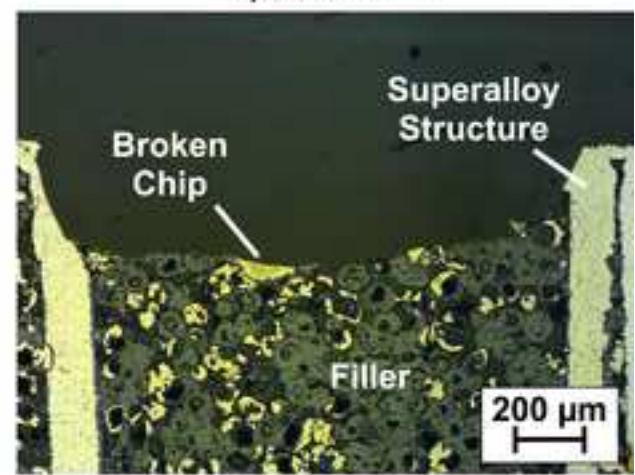
c) Test - Ni+



d) Test - A,S

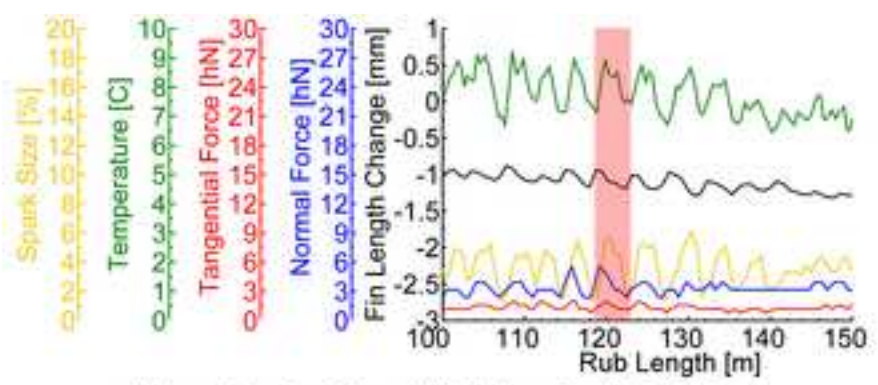


e) Test - A,Al+

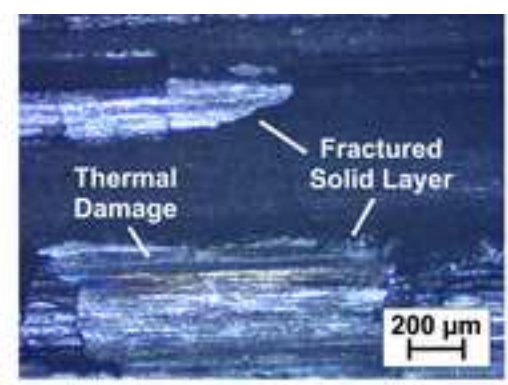


f) Test - A,Ni+

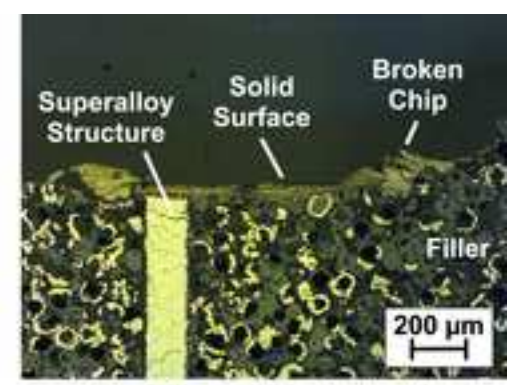
Figure 11



a) Incursion Test Result (Rub Length: 100 - 150 m)



b) Wear Groove Surface View



c) Wear Groove Sectioning View

Table 1

Test Code	Fin Type	Abradable	Tip Speed [m/s]	Incursion speed [$\mu\text{m/s}$]
Test - S	IN718-HVOF	Standard	200	62.1
Test - A,S	IN718-HVOF	Aged standard	200	62.1
Test - Al+	IN718-HVOF	Aluminium rich	200	62.1
Test - A,Al+	IN718-HVOF	Aged aluminium rich	200	62.1
Test - Ni+	IN718-HVOF	Nickel rich	200	62.1
Test - A,Ni+	IN718-HVOF	Aged nickel rich	200	62.1

Table 2

Test Code	Fin Type	Abradable	Tip Speed [ms-1]	Incursion Rate [$\mu\text{m}/\text{pass}$]	Incursion Depth [μm]
Test - S	IN718-HVOF	Standard	200	0.2	2500
Test - A,S	IN718-HVOF	Aged standard	200	0.2	2500
Test - Al+	IN718-HVOF	Aluminium rich	200	0.2	1000
Test - A,Al+	IN718-HVOF	Aged aluminium rich	200	0.2	<1000
Test - Ni+	IN718-HVOF	Nickel rich	200	0.2	1500
Test - A,Ni+	IN718-HVOF	Aged nickel rich	200	0.2	1500

Table 3

Test Number	Ti	Cr	Fe	Co	Ni[1]	Cu
Test - S	0.81	14.35	17.92	1.21	57.75	0.08
Test - A,S	0.97	18.03	18.09	0.56	53.12	0.09
Test - Al+	0.96	19.74	18.11	0.64	50.22	0.08
Test - A,Al+	1.39	25.16	14.71	1.71	47.89	0.16
Test - Ni+	0.00	3.51	3.34	0.38	90.19	0.06
Test - A,Ni+	0.97	18.23	17.77	1.03	52.03	0.07
Fin Base	0.95	16.69	17.33	0.17	47.53	8.17
Fin Tip	0.00	1.27	0.00	2.61	3.37	0.07
Abradable[2]	0.04	5.36	1.65	0.23	90.46	0.08

[1] FISCHERSCOPE® X-RAY XAN® 250 cannot detect aluminium element therefore the nickel content in the ta

[2] The abrasable XRF result present the average value of six different abrasable samples